Computational Modeling of Human Bicuspid Pulmonary Valve Dynamic Deformation in Patients with Tetralogy of Fallot

Caili Li[1, §], Christopher Baird[2], Jing Yao[3], Chun Yang[4], Liang Wang[5], Han Yu[5], Tal Geva[6] and Dalin Tang[5*, 7, §]

Abstract: Pulmonary valve stenosis (PVS) is one common right ventricular outflow tract obstruction problem in patients with tetralogy of Fallot (TOF). Congenital bicuspid pulmonary valve (BPV) is a condition of valvular stenosis, and the occurrence of congenital BPV is often associated with TOF. Dynamic computational models of normal pulmonary root (PR) with tri-leaflet and PR with BPV in patients with TOF were developed to investigate the effect of geometric structure of BPV on valve stress and strain distributions. The pulmonary root geometry included valvular leaflets, sinuses, interleaflet triangles and annulus. Mechanical properties of pulmonary valve leaflet were obtained from biaxial testing of human PV leaflet, and characterized by an anisotropic Mooney-Rivlin model. The complete cardiac cycle was simulated to observe valve leaflet dynamic stress/strain behaviors. Our results indicated that stress/strain distribution patterns of normal tri-leaflet pulmonary valve (TPV) and the BPV were different on valve leaflets when the valve was fully open, but they were similar when valves were completely closed. When the valve was fully open, the BPV maximum stress value on the leaflets was 197.2 kPa, which was 94.3% higher than of the normal TPV value (101.5 kPa). During the valve was fully open, the stress distribution in the interleaflet triangles region of the PR was asymmetric in the BPV model compared with that in the TPV model. The geometric orifice area value in the completely opened position of BPV model was reduced 55.6 % from that of the normal PV. Our initial results demonstrated that valve geometrical variations with BPV may be a potential risk factor linked to occurrence of PVS in patients with TOF. Computational models could be a useful tool in identifying possible linkage between valve disease development and biomechanical factors. Large-scale clinical studies are needed to validate these preliminary findings.

[1]School of Mathematics, Southeast University, Nanjing, 210096, China.

[2]Department of Cardiac Surgery, Boston Children's Hospital, Harvard Medical School, Boston, MA USA.

[3]Department of Cardiology, First Affiliated Hospital of Nanjing Medical University, Nanjing 210029, China.

[4]China Information Tech. Designing & Consulting Institute Co., Ltd., Beijing, 100048, China.

[5]School of Biological Science & Medical Engineering, Southeast University, Nanjing, China.

[6]Department of Cardiology, Boston Children's Hospital, Department of Pediatrics, Harvard Medical School, Boston, MA USA.

[7]Mathematical Sciences Department, Worcester Polytechnic Institute, Worcester, MA USA.

§Li and Tang contributed equally to this paper.

*Corresponding Author: Dalin Tang. Email: dtang@wpi.edu. Southeast University, China.

Keywords: Heart model, pulmonary valve, bicuspid pulmonary valve, tetralogy of Fallot.

1 Introduction

Pulmonary stenosis accounts for approximately 8%-10% of all congenital heart defects and occurs in about one per 2000 live births world-wide [Ruckdeschel and Kim (2018)]. Congenital bicuspid pulmonary valve (BPV) is a condition of valvular stenosis. Its morphologic feature is the presence of only two pulmonary leaflets instead of the normal tri-leaflet. Congenitally BPV are uncommon and the occurrence is often associated with tetralogy of Fallot (TOF) [Nair, Thangaroopan, Cunningham et al. (2006); McAleer, Kurt, Rosenzweig et al. (2001)]. In the reports by Winn et al. [Winn and Hutchins (1973)] and Rao et al. [Rao, Anderson and Edwards (1971)]. BPV where present in 62 (52 %) from 120 TOF patients studied post mortem. In the surgical series by Altrichter, 58% of the pulmonary valves were bicuspid in 65 patients with TOF [Alttichter, Olson, Edwards et al. (1989)]. Similarly, in two necropsy series of patients with TOF, stenotic pulmonary valves were bicuspid in 38% to 55% [Anderson, Allwork, Ho et al. (1981)].

Recent advances in computational modeling techniques are making it possible that computational models can be constructed and used to study valve dynamic mechanical stress and strain behaviors for evaluation of valvular diseases and better design of artificial valves and surgical planning. Effort has been put into developing various innovative surgical options and biomechanical right/left ventricle models in patients with repaired TOF to improve post- pulmonary valve replacement (PVR) outcome and predict right ventricle (RV) function response to PVR [del Nido (2006); Tang, Yang, del Nido et al. (2016); Tang, del Nido, Yang et al. (2016); Zhou, Geva, Rathod et al. (2018)]. Most of the previous work on valve computational modeling was concerned with the mitral valve and the aortic valve in the left ventricle. Kunzelman et al. developed the first three-dimensional (3D) finite element computer model of the mitral valve including leaflets and chordae tendineae. Leaflet and chordal stress and strain and papillary muscle force were determined [Kunzelman, Einstein and Cochran (2007)]. Jermihov et al. performed a dynamic finite element structural analysis of a simulated tri-leaflet aortic valve using four congenital bicuspid aortic valve modles based on geometry published in the literature [Jermihov, Jia, Sacks et al. (2011)]. Their results showed that with the variations of aortic valve geometry, the leaflets stress and strain changed greatly, while changes of the material constants were relatively less. Li et al. [Li and Sun (2010)] proposed a thin pericardial bioprosthetic valve model in which leaflet mechanical properties were obtained from planar biaxial testing of thin bovine and porcine pericardium. In another paper, Sun et al. gave a complete review of computational models for cardiac valves in valve geometry reconstruction, tissue property modeling, and loading and boundary condition definitions [Sun, Martin and Pham (2014)]. Pulmonary valve (PV) function and RV remodeling in TOF patients with pulmonary stenosis by valve-sparing technology were assessed by Hofferberth et al, and their results suggested that valve-sparing repair does not preserve long-term PV function in patients with TOF-PS (tetralogy of Fallot- pulmonary stenosis) [Hofferberth, Nathan, Marx et al. (2018)]. Carreon et al. reviewed the pathological changes of valve venous homografts and their effects on valve function. They pointed out that vascular thickening can cause stenosis [Carreon, Benini, Baird et al. (2018)]. Cuypers et al. [Cuypers, Witsenburg, Van et al. (2013)] provided updated diagnosis and therapeutic options of

pulmonary stenosis. For adult patients of Pulmonary valve stenosis (PVS), Ruckdeschel et al. [Ruckdeschel and Kim (2018)] reviewed the physiology, pathology, clinical management, diagnosis and on isolated forms. Rajiah et al [Rajiah, Nazarian, Vogelius et al. (2014)] and Jonas et al. [Jonas, Kligerman, Burke et al. (2016)] reviewed the normal appearance of the PV as well as various anomalies and variants using a computed tomography and magnetic resonance imaging. Hadeed, et al [Hadeed, Hascoët, Amadieu, et al. (2016)] described the PV morphology and annulus size using 3D transthoracic echocardiography in patients with TOF. All of those gave us basis and basic geometric and physiological data for our model construction and aims for investigations.

Compared with the well-reported computational bicuspid aortic valve models, BPV has been under-investigated. In this paper, computational models for normal pulmonary root (PR) with tri-leaflet and PR with BPV in patients with TOF were constructed to simulate valve dynamic motions and investigate the effect of BPV geometric structure on its stress and strain distribution.

2 Methods

2.1 The 3D geometric model of the pulmonary root

Pulmonary root is the part of the right ventricular outflow tract that supports the leaflets of the pulmonary valve [Anderson, Razavi and Taylor (2004)]. The entire PR structure includes valvular leaflets, sinuses, interleaflet triangles and annulus which are illustrated by Figs. 1(a)-1(c). The 3D geometric reconstruction of PR was based on well-accepted analytic models [Conti, Votta, Corte, et al. (2010); Haj-Ali, Marom, Zekry et al. (2012)] with physiological parameters obtained from a typical sample of the pulmonary root used in clinical surgery (Fig. 1(a)). Details are given below:

2.1.1 The sinuses and interleaflet triangles

To demonstrate how the 3D sinus and interleaflet triangles geometry was constructed, we start from a slice (Fig. 1(d)) and provide analytic equations which were used to generate the slice contours. Each slice was made by one base circle, superimposed by 3 smaller circles, each replacing a part of the base circle to generate the sinus (the part that bulged out and shown by blue line shown in Fig. 1(d)) and interleaflet triangle (the part that not bulged out of the blue line shown in Fig. 1(d)) . The equation of the base circle C_0 is given by:

$$P_0 = [\tfrac{1}{2}D_a\cos\theta, \tfrac{1}{2}D_a\sin\theta, H], \theta \in [0, 2\pi], \tag{1}$$

where H is the height of the slice, D_a is the diameter of the circle C_0. Here we assume that the diameter of the annulus is also D_a. The parametric equations of the three smaller circles $C_1, C_{2,}C_3$ are given by:

$$P_1 = [R_{IS}\cos\theta + R\cos\tfrac{\pi}{3}, R_{IS}\sin\theta + R\sin\tfrac{\pi}{3}, H] \tag{2}$$

$$P_2 = [R_{IS}\cos\theta - R, R_{IS}\sin\theta, H] \tag{3}$$

$$P_3 = [R_{IS}\cos\theta + R\cos(-\tfrac{\pi}{3}), R_{IS}\sin\theta + R\sin(-\tfrac{\pi}{3}), H] \tag{4}$$

where,

$$R_{IS} = (R_m - D_s + D_a) + R_I - D_a/2 \tag{5}$$

$$R_I = \sqrt{R_m^2 - (H - \tfrac{1}{2}H_{STJ})^2} - (R_m - D_s + D_a/2) \tag{6}$$

$$R = D_s - D_a/2 - R_m \tag{7}$$

$$R_m = \tfrac{1}{2}[(D_s - D_a)^2 + (\tfrac{1}{2}H_{STJ})^2]/(D_s - D_a) \tag{8}$$

where H_{STJ} is the height of sinutubular junction, D_s is maximum inner diameter of sinus. The points on the circle C_1, C_2, C_3 and C_0 are selected and smoothed with $p_{i,}(i = 1, \cdots, 6)$ as the demarcation points to obtain the some slices of the sinuses and interleaflet triangles given by the blue line in Fig. 1(e) which were used to construct the 3D sinuses and interleaflet triangles geometry. The coordinates of the sinus and interleaflet triangle outer point (P_{out}) (the red line shown in Fig. 1(e)) are as follows:

$$P_{out} = \left[\left(1 + T_a/\sqrt{x_0^2 + y_0^2}\right)x_0, \left(1 + T_a/\sqrt{x_0^2 + y_0^2}\right)y_0, H\right] \tag{9}$$

where T_a is the thickness of sinus wall.

2.1.2 The leaflets of PV

We assume that three leaflets are symmetrical and take a slice of the left leaflet as an example to illustrate the geometry generation process. The intersection points of the inner edge of the left leaflet and sinus $p_1(s_1, t_1, H_v)$ and $p_2(s_2, t_2, H_v)$ (see Fig. 1(d)), and inner points $(V_{i,}(x_i, y_i, H_v)(i = 1, \cdots, n))$ of left leaflet are given as follows:

$$V_i = [r(x_i' \cos\alpha - y_i' \sin\alpha), r(x_i' \sin\alpha + y_i' \cos\alpha), H_v], i = 1, \cdots, n \tag{10}$$

$$V_i = \left[x_i - \tfrac{1}{2}(x_1 + x_n) + \tfrac{1}{2}(s_2 + s_1), y_i - \tfrac{1}{2}(y_1 + y_n) + \tfrac{1}{2}(t_2 + t_1), H_v\right], i = 1, \cdots, n \tag{11}$$

Where,

$$y_i' \in [-\tfrac{\sqrt{3}}{4}D_a, \tfrac{\sqrt{3}}{4}D_a] \ , \ x_i' = \left|\tfrac{1}{\sqrt{3}}y_i'\right|, i = 1, \cdots, n \tag{12}$$

$$r = |p_1 - p_2|/(\sqrt{(x_1' - x_n')^2 + (y_1' - y_n')^2}) \ , \ \alpha = \tan^{-1}\left(-\tfrac{s_2 - s_1}{t_2 - t_1}\right) \tag{13}$$

$H_v = H$ and $H_v \leq H_E$, where H_E is the effective height of the valve. For the outer points of the left leaflet, the intersection points of the outer edge of the left leaflet and sinus are obtained according to the thickness of the leaflet. The process is the same as that of the inner points. The green line in Fig. 1(e) represents the leaflets.

The contours of PR with different axial heights used to construct the PR and the valve are shown in Figs. 1(g) and 1(h). The valve geometry is similar to the other artificial or native valves reported in the literature [Conti, Votta, Corte et al. (2010); Rajiah, Nazarian, Vogelius et al. (2014); Anderson, Razavi and Taylor (2004); Jonas, Kligerman, Burke et al. (2016)]. The normal PR with tri-leaflet pulmonary valve (TPV) geometry with zero-load was reconstructed, and the construction process and model parameters for PR geometry with zero-load are shown in Fig. 1 and Tab. 1, respectively.

Previous studies have documented that BPV were common in TOF patients [Nair, Thangaroopan, Cunningham et al. (2006); McAleer, Kort, Rosenzweig et al. (2001); Chacko, Chiramel, Vimala et al. (2017)]. Their data reported that 81% of bicuspid valves did not have a median raphe [Chacko, Chiramel, Vimala et al. (2017)]. Based on those studies, a computational BPV geometry using a typical TOF patient parameters was created as shown in Fig. 1(j). In our model of PR with BPV, the geometry of BPV is that there are only two leaflets fused without median raphe. The selection of geometric parameters of the model is the same as that of normal TPV.
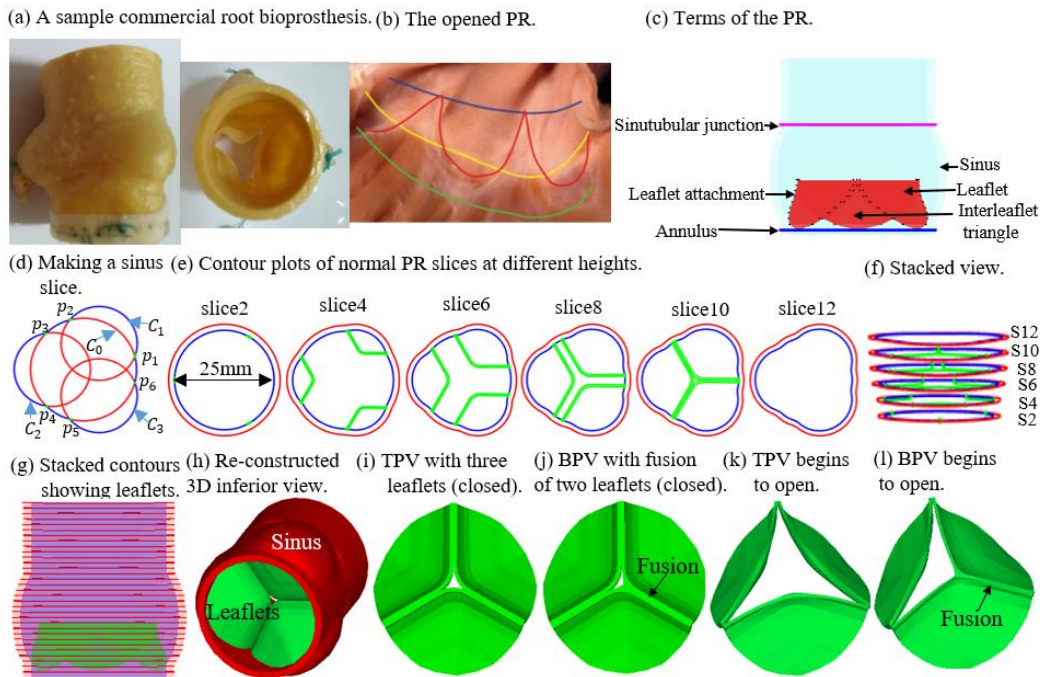

Figure 1: The TPV and BPV PR model construction process and zero-load geometry. (a) a sample commercial root bioprosthesis; (b) the opened PR with the leaflets removed [Anderson, Razavi and Taylor (2004)]; (c) Terms of the PR. (d) making a sinus slice; (e) contour plots of normal PR slices at different heights; (f) Stacked view of the some contours; (g) Sstacked contours showing leaflets; (h) Re-constructed 3D inferior view; (i) TPV with three leaflets (closed); (j) BPV with fusion of two leaflets (closed); (k) TPV begins to open; (l) BPV begins to open

Table 1: Model parameters for PR geometry with zero-load

Parameter	Values
Inner diameter of sinutubular junction	25 mm
Inner diameter of annulus	25 mm
Maximum inner diameter of sinus	28 mm
Height of sinutubular junction	20 mm
Effective height of the valve	9.0 mm
Thickness of the leaflet	0.4 mm
Thickness of the pulmonary artery	1.5 mm

2.2 Pulmonary valve material properties

Biaxial mechanical testing was performed using a healthy human cadaver PV leaflet sample to obtain PV leaflet material properties. The biaxial mechanical testing procedures were described in Sun et al. [Sun, Sacks, Sellaro et al. (2003); Li and Sun (2010)]. Briefly, Human pulmonary valve leaflet sample were immersed in phosphate buffered normal saline for biaxial tension test at room temperature. Firstly, at least 20 equal-biaxial stretch cycles were performed to make the maximum Lagrangian stress level of 1 MPa at the stress loading rate of 40 kPa/s. Then, the subsequent test schemes are implemented by using constant Lagrangian normal stress ratios of 0.3:1, 0.5:1, 0.75:1, 1:1, 1:0.75, 1:0.5 and 1:0.3. For the material models, we assumed that the PV material is hyperelastic, nearly incompressible, and anisotropic (valvular leaflets)/isotropic (sinuses). The Mooney-Rivlin model was used to describe the nonlinear anisotropic and isotropic material properties. The strain energy function for the isotropic modified Mooney-Rivlin model is given below [Tang, Yang, del Nido et al. (2016); Tang, del Nido, Yang et al. (2016); Anderson, Razavi and Taylor (2004)]:

$$W = c_1(I_1 - 3) + c_2(I_2 - 3) + D_1[e^{D_2(I_1-3)} - 1] \tag{14}$$

where I_1, and I_2 are the first and second strain invariants,

$$I_1 = \sum C_{ii}, \ I_2 = \frac{1}{2}(I_1^2 - C_{ij}C_{ij}), \ i,j = 1,2,3, \tag{15}$$

$C = [C_{ij}] = F^T F$ is the right Cauchy-Green deformation tensor. $F = [X_{ij}] = [\partial x_i / \partial a_j]$ where x_i is the current location and a_j is the original location. c_1, c_2, D_1, and D_2 are the material parameters and were chosen to match experimental measurements [Tang, Yang, Geva et al. (2011)]. The strain energy function for the anisotropic modified Mooney-Rivlin model is given as:

$$W = c_1(I_1 - 3) + c_2(I_2 - 3) + D_1(e^{D_2(I_1-3)} - 1) + \frac{K_1}{K_2}(e^{K_2(I_4-1)^2} - 1) \tag{16}$$

where $I_4 = C_{ij}(n_f)_i(n_f)_j$, C_{ij} is the Cauchy-Green deformation tensor, n_f is the fiber direction, K_1 and K_2 are the material parameters. A least-squares method was used to determine the parameter values in (3) to fit the biaxial mechanical testing data provided by Professor Wei Sun at Georgia Institute of Technology. By choosing the valve radial and circumferential directions as the local coordinate axes, the stress was implemented in circumferential, radial direction during the test. Noticing that $\lambda_c \lambda_r \lambda_a = 1, \lambda$ is the stretch

ratio in the circumferential, radial and pulmonary artery (PA) axial directions, λ_c, λ_r and λ_a represent circumferential, radial and axial stretch, respectively. $\sigma = J^{-1}FTF^{-1}$ where σ is Cauchy stress, T is the second Piola-Kirchhoff stress, and $T_{cc} = \partial W/\partial E_{cc}$, $T_{rr} = \partial W/\partial E_{rr}$, where $E_{ij} = 1/2(C_{ij} - \delta_{ij})$ is the Green Strain tensor, and δ_{ij} is the Kronecker delta, we assume that the direction of the fibers is circumferential, we obtain from (16):

$$\sigma_c = 2c_1 C_{cc}\left(1 - \frac{1}{C_{cc}{}^2 C_{rr}}\right) + 2D_1 D_2 C_{cc}\left(1 - \frac{1}{C_{cc}{}^2 C_{rr}}\right) + 4K_1 C_{cc}(I_4 - 1)e^{K_2(I_4-1)^2}$$

$$+ 2c_2 C_{cc}\left(C_{rr} - \frac{1}{C_{cc}{}^2}\right) \qquad (17)$$

$$\sigma_r = 2c_1 C_{rr}\left(1 - \frac{1}{C_{rr}{}^2 C_{cc}}\right) + 2D_1 D_2 C_{rr}\left(1 - \frac{1}{C_{rr}{}^2 C_{cc}}\right)e^{D_2(I_1-3)} + 2c_2 C_{rr}\left(C_{cc} - \frac{1}{C_{rr}{}^2}\right) \quad (18)$$

where C_{cc}, C_{rr} are components of the right Cauchy-Green deformation tensor .Using stress values obtained from the biaxial testing, we define

$$H_{D_2,K_2}(c_1, c_2, D_1, K_1) = \Sigma\left(\sigma_c - \sigma_c^{exp\ data}\right)^2 + \Sigma\left(\sigma_r - \sigma_r^{exp\ data}\right)^2 \qquad (19)$$

With D_2 and K_2 fixed, least square approximation technique was used to minimize $H_{D_2,K_2}(c_1, c_2, D_1, K_1)$ to obtain c_1, c_2, D_1 and K_1 (all functions of D_2, K_2). Then let D_2 and K_2 change from -100 to100, we perform the last step to get the corresponding c_1, c_2, D_1 and K_1 values, and the fitting error (the H value) for all (D_2, K_2) combinations with initial increment=10. Optimal (D_2, K_2) and the associated c_1, c_2, D_1 and K_1 values were determined by choosing the pair corresponding to a minimum H value. Searching increment for (D_2, K_2) starts from 10 for [-100,100] and then refines to 1, and 0.1 when search domain is reduced. The parameter values determined for the sample were: c_1=1.0529 kPa, c_2=-3.7637, D_1=3.0899 kPa, D_2=1.5, K_1=0.6615 kPa, K_2=5.3138. Fig. 2 plots the biaxial data with all 7 stretch-ratio results, in which the black line curves are the fitting curves given by the Mooney-Rivlin model and the colored marks representing the experimental biaxial mechanical testing data. It should be noted that the curves are 3D with the second stretch axis on the right end of the coordinate frames.
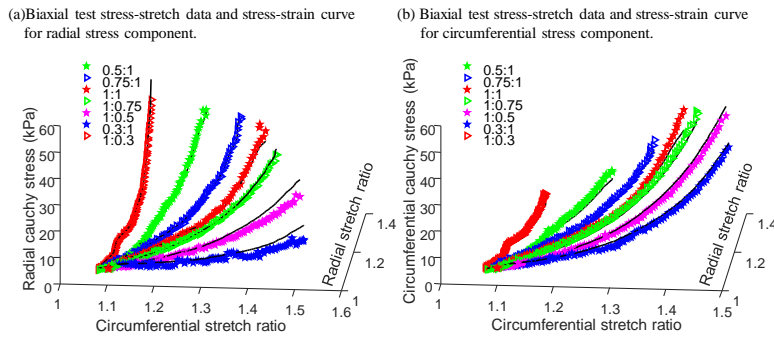

(a)Biaxial test stress-stretch data and stress-strain curve for radial stress component.

(b) Biaxial test stress-stretch data and stress-strain curve for circumferential stress component.

Figure 2: Biaxial mechanical testing data of a healthy cadaver PV leaflet sample was obtained to fit Mooney- Rivlin model. The 7 Radial: Circumferential stress ratios are: 0.3:1,

0.5:1, 0.75:1, 1:1, 1:0.75, 1:0.5 and 1:0.3. (a) Biaxial test stress-stretch data and stress-strain curve for radial stress component. (b) Biaxial test stress-stretch data and stress-strain curve for circumferential stress component

2.3 Governing equations and boundary conditions

The governing equations for pulmonary root models were as follows:

$$\rho v_{i,tt} = \sigma_{ij,j}, \quad i,j = 1,2,3, \tag{20}$$

$$\varepsilon_{ij} = (v_{i,j} + v_{j,i} + v_{\alpha,i}v_{\alpha,j})/2, \quad i,j,\alpha = 1,2,3, \tag{21}$$

$$p|_{RV} = p|_{RV}(t), p|_{PA} = p|_{PA}(t), \tag{22}$$

where σ is the stress tensor, ρ is the material density, ε is the strain tensor, v is displacement, and p is the pressure. Since it is a structure-only model, RV pressure was imposed on the RV side of leaflets; and PA pressure was imposed on the PA side of the leaflets. If flow were included, those pressure conditions would be imposed at the inlet and outlet of the PR. The normal stress was assumed to be zero on the outer (epicardial) PR surface and the pressure conditions imposed on the inner (endocardial) PR and valvular leaflets surfaces. These models provided valvular leaflets and PR stress/strain values, and geometric orifice area for analysis.

Our valve models were solved using a commercial finite element package ADINA (ADINA R & D, Watertown, MA USA). In our models, leaflet contact was simulated with three pairs of leaflet RV side edges defined as "contact surfaces" using the contact settings in ADINA. Contact in ADINA is modeled using contact groups, contact surfaces, contact segments and contact pairs. Specific settings are as follows: (1) contact groups (and their contact surfaces) are 3-D. (2) Single-sided contact surface and large displacement contact are selected. (3) Constraint functions are used to enforce the no-penetration and the frictionless contact conditions. (4) Setting the Newmark parameter $\alpha = 0.5$ to reduce numerical oscillation in flexible leaflets contact. A closed configurations of the leaflets were shown by Fig. 1(i) and Fig. 1(j)) which were chosen as the zero-load initial configuration.

Dynamic deformation of leaflets from closure to complete opening and then from open to complete closure was achieved by imposing RV pressure condition at the RV side of the leaflets and a pressure profile adjusted from PA pressure condition at the PA side of the leaflets. The RV pressure curve was obtained from one sample TOF patient obtained from cardiac catheterization procedures (NIH project, 1R01-HL089269). Pulmonary artery pressure conditions were assigned using available literature and adjusted so that PV would have proper open and close motions [Hioka, Kaga, Mikami et al. (2017); Whitener, Konoske and Mark (2014)]. The imposed pressure profiles are shown in Fig. 3. It should be noted that the exact pressure conditions acting on the two sides of the leaflets are very hard to measure and fluid-structure interaction models should be used to get more accurate results using RV and PA pressure conditions.
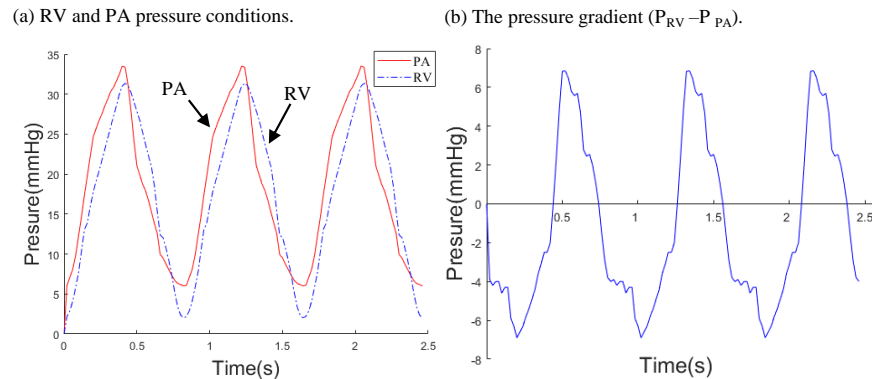
Figure 3: Imposed pressure conditions for the PR models. (a) Right ventricle (RV) and pulmonary artery (PA) pressure conditions imposed in the PR model; (b) The pressure gradient ($P_{RV} - P_{PA}$)

2.4 Mesh generation, solution methods and simulation procedures

Volume component-fitting method was employed to generate meshes for PR with complex geometry [Yang, Tang and Haber (2007); Tang, Yang and Geva (2008); Fan, Yao, Yang et al. (2018)]. In this approach, the valve leaflets and PR were divided into many blocks or pieces (called "volume" by ADINA) such that each volume has a more regular shape which is easier for mesh generation. Mesh density and mesh style were specified for each volume to generate the final mesh in ADNIA (Fig. 4). The anisotropic computational models were constructed for PR with TPV and PR with BPV and the models were solved by ADINA (ADINA R&D, Watertown, MA, USA) using unstructured finite elements and the Newton-Raphson iteration method [Tang, Yang and Geva (2008)]. Stress/strain distributions were computed. The time for a cardiac cycle was 0.82 s. Three cardiac cycles were simulated and the solution for the third cycle was almost identical to the second cycle. Therefore, the third cycle was selected as the final solution and used for comparison and numerical analysis. Mesh analysis was performed by increasing mesh density in each dimension by 10% incrementally until the solutions became mesh independent. Because stress and strain are tensors, for simplicity, maximum principal stress (Stress-P_1) and strain (Strain-P_1) were used and referred to as stress and strain in this paper.
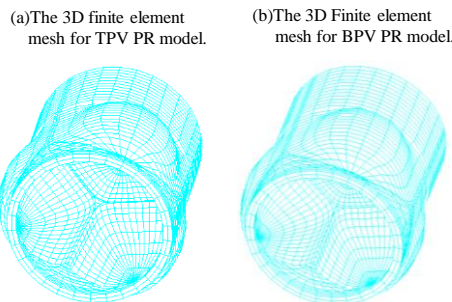

Figure 4: The 3D finite element mesh for TPV and BPV PR model

3 Results

We will analyze differences between normal TPV and BPV from three aspects: a) stress/strain distribution on the leaflets; b) stress/strain distribution on pulmonary root; and c) the geometric orifice area. Details are given below.

3.1 When the valve was fully open, the BPV maximum stress value on the leaflets was 94.3% higher than of the normal TPV

Figs. 5 and 6 gave stress/strain plots on the leaflets for the normal TPV and BPV with the leaflets at 8 key time points in one cardiac cycle: begin-diastole, rapid filling period, slow down filling period, end-diastole, begin-systole, peak-systole, slow ejection period and end-systole. Our results indicated that stress/strain distribution patterns of normal TPV and the BPV were different on valve leaflets when the valve was open. At peak-systole when the valve was fully open, BPV maximum Stress-P_1 on the leaflets was 197.2 kPa, 94.3% higher than that from the normal TPV leaflet (101.5 kPa). The location of the maximum Stress-P_1 from TPV and BPV were also different, which were found at the bottom of the valve near the leaflet attachment for TPV and the vicinity of cusp of the fusion of two leaflets for BPV, respectively. When the valve was closed, stress/strain distribution patterns on valve leaflets were similar for the TPV and BPV models. Fig. 6 showed maximum Strain-P_1 from BPV leaflet at peak-systole was 0.712, 70.7% higher than that from the normal TPV.

3.2 The BPV pulmonary root stress in the interleaflet triangles region is more asymmetric compared to TPV stress

Taking the vertical axis (the z-axis) as the "symmetry axis", TPV geometry has a 120° rotation symmetry, i.e., the geometry repeats with a 120° rotation. We chose a view angle where 2 leaflets from the TPV model are symmetric to show the symmetry/asymmetry. Stress-P_1 distributions for PR with TPV and PR with BPV at their fully open positions are show in Fig. 7. When the valve was fully open, Stress-P_1 distribution patterns of TPV model in the interleaflet triangles region was essentially symmetrical (see the first row of Fig. 7) while that of BPV model was asymmetrical (see the second row of Fig. 7). In particular, the interleaflet triangle region between the anterior and left leaflets is significantly asymmetrical. Stress-P_1 on the side near the anterior leaflet is greater and Stress-P_1 on the left leaflet is smaller, which may be related to the fusion of the left and right leaflets (Fig. 7(a)). This asymmetry indicates that BPV may be one of the causes post-stenotic PA dilatation and aneurysm in patients with PV malformation such as TOF. Meanwhile, peak Stress-P_1 of BPV was observed at the vicinity of cusp of the fusion of two leaflets with the value about 204.3 kPa, and the peak Stress-P_1 of TPV was found at the junction between bottom of leaflet and annulus with the value about 127.2 kPa. The largest change on the PR with the geometrical variations in the 2 models was 60.6% in maximum Stress-P_1.

3.3 Compared with normal TPV, the geometric orifice area in the completely open position for BPV is significantly reduced

Valve opening was assessed by geometric orifice area. The time-varying opening area was calculated from end-diastole to end-systole, as shown in Fig. 8. The open area (Fig. 8(a)) is similar to that reported in literature [Jermihov, Jia, Sacks et al. (2011); Murdock, Martin

and Sun (2018)]. Due to the abnormal morphology of the valve caused by fusion of the two leaflets, the cusp showed significant eccentricity during peak systolic period (see Fig. 8(a)). Compared to normal TPV, the geometric orifice area in the valve opened position of the congenital BPV is significantly reduced (see Fig. 8(d)). When the valve was fully open, the BPV valve geometric orifice area was $2.0 \, \text{cm}^2$, which is a 55.6% reduction of the normal TPV value ($4.5 \, \text{cm}^2$). This has a huge impact on valve functions.

(a) Stress-P_1 plots from the TPV model.

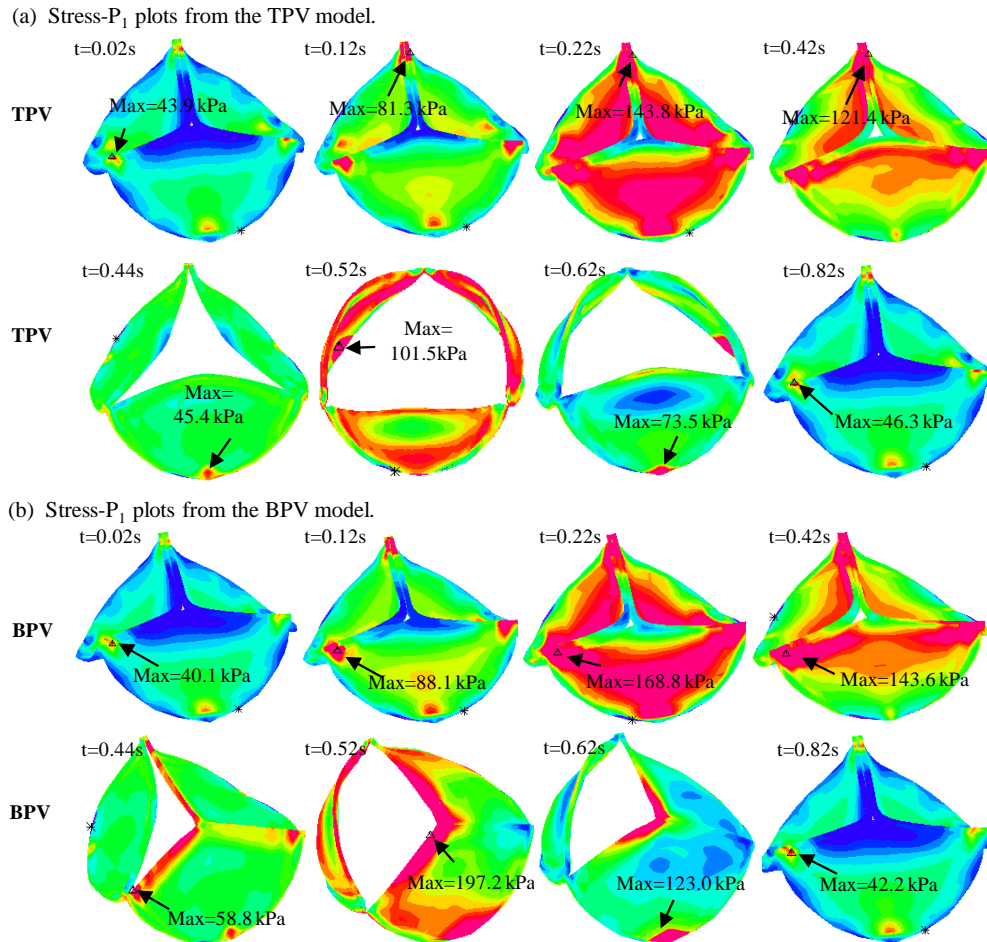(b) Stress-P_1 plots from the BPV model.

Figure 5: Stress-P_1 plots for the TPV and BPV leaflets in a cardiac cycle. (a): Stress-P_1 plots from the TPV model; (b) Stress-P_1 plots from the BPV model. t=0.02 s, begin-diastole, tricuspid valve begins to open, pulmonary valve (PV) closed; t=0.12 s, rapid filling period, tricuspid valve open, PV closed; t=0.22 s, slow down filling period, tricuspid valve open, PV remains closed; t=0.42 s, end-diastole: t=0.42 s, both valves closed; t=0.44 s, begin-systole, tricuspid valve closed, PV opens; t=0.52 s, peak-systole, tricuspid valve closed, PV fully open; t=0.62 s, slow ejection period, tricuspid valve closed, PV open; t=0.82 s, end-systole: tricuspid valve closed, PV completely closed
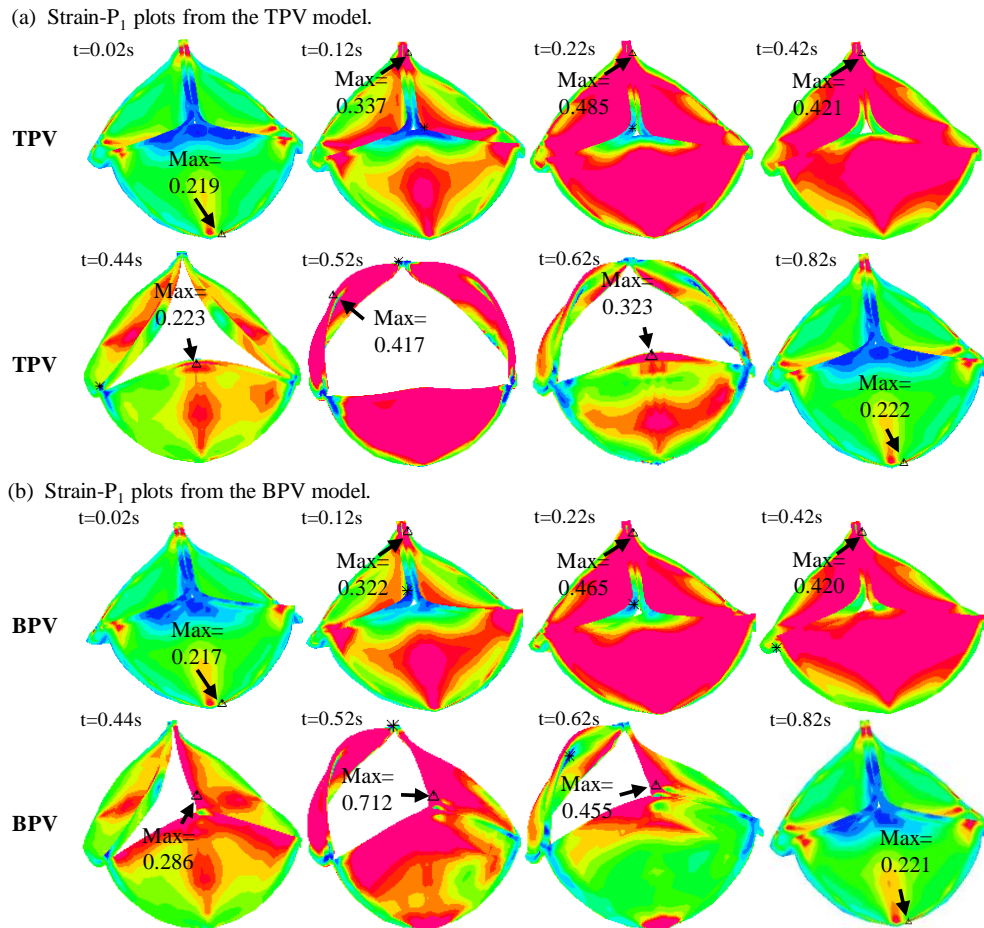
Figure 6: Strain-P$_1$ plots for the TPV and BPV leaflets in a cardiac cycle. (a) Strain-P$_1$ plots from the TPV model; (b) Strain-P$_1$ plots from the BPV model. t=0.02 s, begin-diastole, tricuspid valve begins to open, pulmonary valve (PV) closed; t=0.12 s, rapid filling period, tricuspid valve open, PV closed; t=0.22 s, slow down filling period, tricuspid valve open, PV remains closed; t=0.42 s, end-diastole: t=0.42 s, both valves closed; t=0.44 s, begin-systole, tricuspid valve closed, PV opens; t=0.52 s, peak-systole, tricuspid valve closed, PV fully open; t=0.62 s, slow ejection period, tricuspid valve closed, PV open; t=0.82 s, end-systole: tricuspid valve closed, PV completely closed

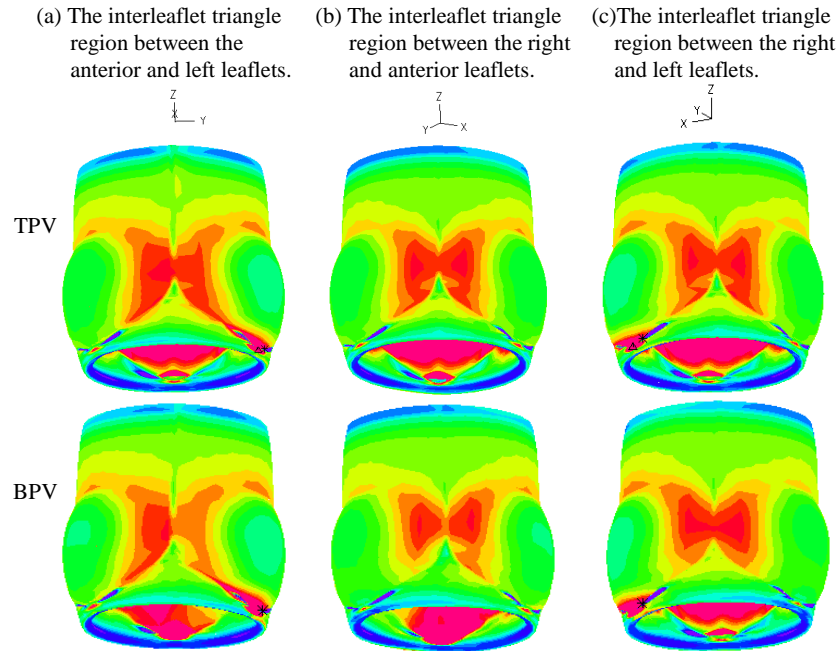**Figure 7:** Stress-P_1 plots for PR with TPV and BPV in a fully open position. (a) The interleaflet triangle region between the anterior and left leaflets; (b) the interleaflet triangle region between the right and anterior leaflets; (c) the interleaflet triangle region between the right and left leaflets
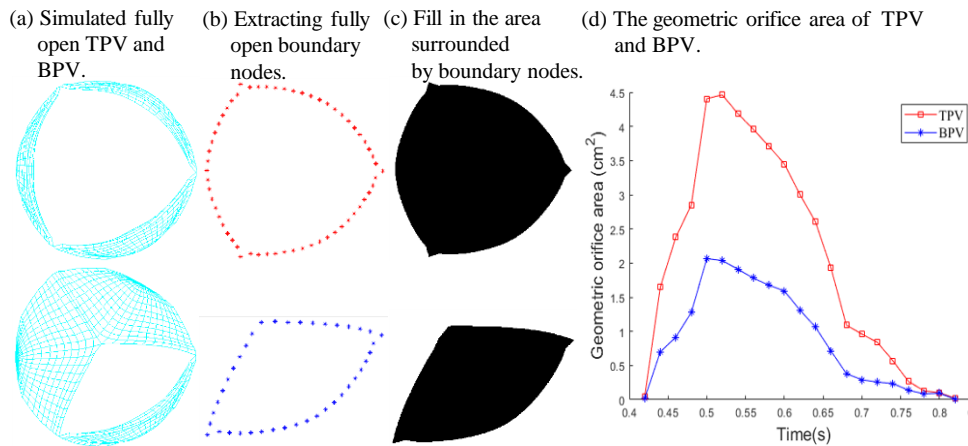

Figure 8: Top view of valve orifice area in the x-y plane exported from the normal TPV and BPV. (a) Top view snapshot of the full opening valve exported from the simulation normal TPV and BPV; (b) Top-view snapshot of the full opening valve after extracting boundary nodes of normal TPV and BPV; (c) Fill in the area surround by boundary nodes to measure the geometric orifice area of normal TPV and BPV; (d) The geometric orifice area of the normal TPV and BPV in simulation from end-diastole to end-systole

4 Discussion

This is a proof-of-the-concept initial effort using computational models to simulate valve mechanics with two examples seeking potential clinical applications. The general significance is that if the modeling approach could be validated and accepted, it could be used as an effective tool to test new valve designs, valve materials and new surgical procedures without testing those on patients. The mechanical analysis could also be useful in disease development investigations.

4.1 Computational valve model as a tool for potential use in studying valve mechanics

This study developed a normal PR model with tri-leaflet and a PR model with BPV in patients with TOF to study the kinematic opening and closing behavior of the valve in a complete cardiac cycle. While computational models have been used in bicuspid aortic valve biomechanical analysis, it has not been used to evaluate congenital BPV in patients with TOF. We developed anisotropic models of PR with material properties of the human PV leaflet tissue derived from in-vitro biaxial testing and characterized by an anisotropic hyperelastic material model. We also calculated the stress/strain distribution of the valve during the opening and closing phases of the entire cardiac cycle under the same pressure for TPV and BPV models. There are clearly significant differences in stress/strain distributions between TPV and BPV PR models. The models and results could serve as basis for further valve mechanics and valve disease initiation and development research.

4.2 Clinical significance of abnormal BPV mechanical features

Our results demonstrated that stress distribution in the interleaflet triangles region of the BPV PR is asymmetric compared to that in the TPV PR model when the valve was fully open. The BPV PR maximum stress could be 60.6% higher than that from TPV PR model. This stress asymmetry indicates that BPV may be one of the causes of pulmonary artery dilatation and aneurysm in patients with PV malformation such as TOF. It has been reported that BPV is associated with post-stenotic pulmonary arterial dilation and aneurysm [Fenster, Schroeder, Hertzberg et al. (2012)]. The mechanisms how mechanical conditions could be associated with the initiation and development of post-stenotic pulmonary artery dilatation and aneurysm need further investigations. Computational BPV models could provide new insights into the relationship between mechanics (PR stress and strain) and the abnormal two-leaflet pattern of PV in TOF. To our knowledge, this is the first study assessing PR with BPV in TOF patients using computational simulation models.

Valve opening was assessed by geometric orifice area, so the time-varying opening area was calculated from end-diastole to end-systole. Our simulations showed that the geometric orifice area of BPV was significantly reduced compared to TPV during the period of valve opening. The maximum geometric orifice area reduction of BPV was as high as 55.6% when the valves were completely open. The result is in the same range of the percentage values reported in Conti et al (51%, the diameter of the annulus is 23 mm) [Jermihov, Jia, Sacks et al. (2011)]. The impact of this area reduction should be investigated using full coupled ventricle-valve fluid-structure interaction (FSI) models.

4.3 Limitations

Our first major limitation is that image-based patient-specific 3D valve geometry reconstruction was not included and data from root bioprosthesis and existing literature were used [Cuypers, Witsenburg, Van et al. (2013); Rajiah, Nazarian, Vogelius et al. (2014); Jonas, Kligerman, Burke et al. (2016)]. Obtaining patient-specific geometric structure of pulmonary root, especially pulmonary valve is not routinely done in clinical cardiac imaging. Medical imaging lacks sufficient resolution to provide accurate information on the thickness of the valve structure. Reconstructing the 3D geometry of the pulmonary root based on patient-specific will be our next step in our research direction.

Our second major limitation is that FSI was not included. Fluid-structure interaction models not only capture the interaction between the valve leaflets and the blood in a more realistic way, but also exhibit flow shear stress on the pulmonary root wall and surface of the valve leaflets [Luraghi, Migliavacca and Matas (2018); Bavo, Rocatello, Iannaccone et al. (2016)]. While valve opening and closing are controlled by the pressure conditions imposed on the two sides of the valve leaflets, the exact pressure conditions acting on the two sides of the leaflets are very hard to measure and fluid-structure interaction models should be used to get more accurate results using RV and PA pressure conditions. Since we had structure-only model, the pressure conditions imposed at the inlet and outlet of the PR were the same as those on the RV side and PA side of the leaflets. That would not be true if flow were included. Thus, FSI models are desirable to have. Fluid-structure interaction models would allow us to use RV and PA pressure conditions as boundary conditions and we would be able to obtain both structural stress/strain and flow shear stress conditions. Flow shear stress plays an important role in valve disease development and worsening. The Arbitrary Lagrangian-Eulerian (ALE)-based FSI guarantees very accurate results near the interface between the solid structures and the fluid, but it is facing some challenges when used for heart valve simulation. Remeshing leads to high computational cost. Excessive deformation of fluid grid leads to convergence difficulties. The most significant challenge is dealing with the connection of fluid fields during valve closure [Luraghi, Migliavacca and Matas (2018)]. Fully coupled fluid-structure coupling method to simulate the dynamic analysis of pulmonary root will be our future effort.

5 Conclusion

Dynamic computational models of normal PR with TPV and PR with BPV in patients with TOF in the entire cardiac cycle was developed. The dynamic computational model demonstrated that stress on the leaflets and PR of the valve in BPV patients is different from that in normal TPV, and geometrical variations with BPV may be a potential risk factor linked to occurrence of PVS in patients with TOF. Computational models could be a useful tool in identifying possible linkage between valve disease development and biomechanical factors.

References

Alttichter, P. M.; Olson, L. J.; Edwards, W. D.; Puga, F. J.; Danielson, G. K. (1989): Surgical pathology, of the pulmonic valve: a study of 116 cases spanning 15 years. *Mayo Clinic Proceedings*, vol. 64, no. 11, pp. 1352-1360.

Anderson, R. H.; Allwork, S. P.; Ho, S. Y.; Lenox, C. C.; Zuberbuhler, J. R. (1981): Surgical anatomy of tetralogy of Fallot. *Journal of Thoracic and Cardiovascular Surgery*, vol. 81, no. 6, pp. 887-896.

Anderson, R. H.; Razavi, R.; Taylor, A. M. (2004): Cardiac anatomy revisited. *Journal of anatomy*, vol. 205, no. 3, pp. 159-177.

Bavo, A. M.; Rocatello, G.; Iannaccone, F.; Degroote, J.; Vierendeels, J. et al. (2016): Fluid-structure interaction simulation of prosthetic aortic valves: comparison between immersed boundary and arbitrary lagrangian-eulerian techniques for the mesh representation. *PLoS One*, vol. 11, no. 4, e0154517.

Carreon, C. K.; Benini, A.; Baird, C.; Hoganson, D.; Borisuk, M. et al. (2018): Pathology of valved venous homografts used as right ventricle-to-pulmonary artery conduits in congenital heart disease surgery. *Journal of thoracic and cardiovascular surgery*, vol. 157, no. 1, pp. 342-350.

Chacko, B. R.; Chiramel, G. K.; Vimala, L. R.; Manuel, D. A.; Joseph, E. et al. (2017): Spectrum of pulmonary valve morphology and its relationship to pulmonary trunk in tetralogy of Fallot. *Indian Journal of Radiology & Imaging*, vol. 27, no. 1, pp. 65-69.

Conti, C. A.; Votta, E.; Della Corte, A.; Del Viscovo, L.; Bancone, C. et al. (2010): Dynamic finite element analysis of the aortic root from MRI-derived parameters. *Medical Engineering & Physics*, vol. 32, no. 2, pp. 212-221.

Cuypers, J. A.; Witsenburg, M.; Van der Linde, D.; Roos-Hesselink, J. W. (2013): Pulmonary stenosis: update on diagnosis and therapeutic options. *Heart*, vol. 99, no. 5, pp. 339-347.

Del Nido, P. J. (2006): Surgical management of right ventricular dysfunction late after repair of tetralogy of fallot: right ventricular remodeling surgery. *Seminars in Thoracic and Cardiovascular Surgery: Pediatric Cardiac Surgery Annual*, vol. 9, no. 1, pp. 29-34.

Fan, L.; Yao, J.; Yang, C.; Xu, D.; Tang, D. (2018): Patient-specific echo-based fluid-structure interaction modeling study of blood flow in the left ventricle with infarction and hypertension. *Computer Modeling in Engineering & Sciences*, vol. 114, no. 2, pp. 221-237.

Fenster, B. E.; Schroeder, J. D.; Hertzberg, J. R.; Chung, J. H. (2012): 4-Dimensional cardiac magnetic resonance in a patient with bicuspid pulmonic valve: characterization of post-stenotic flow. *Journal of the American College of Cardiology*, vol. 59, no. 25, pp. 49.

Hadeed, K.; Hascoët, S.; Amadieu, R.; Dulac, Y.; Breinig, S. et al. (2016): 3D transthoracic echocardiography to assess pulmonary valve morphology and annulus size in patients with tetralogy of Fallot. *Archives of Cardiovascular Diseases*, vol. 109, no. 2, pp. 87-95.

Haj-Ali, R.; Marom, G.; Zekry, S. B.; Rosenfeld, M.; Raanani, E. (2012): A general three-dimensional parametric geometry of the native aortic valve and root for biomechanical modeling. *Journal of Biomechanics*, vol. 45, no. 14, pp. 2392-2397.

Hioka, T.; Kaga, S.; Mikami, T.; Okada, K.; Murayama, M. et al. (2017):

Overestimation by echocardiography of the peak systolic pressure gradient between the right ventricle and right atrium due to tricuspid regurgitation and the usefulness of the early diastolic transpulmonary valve pressure gradient for estimating pulmonary artery pressure. *Heart Vessels*, vol. 32, no. 7, pp. 833-842.

Hofferberth, S. C.; Nathan, M.; Marx, G. R.; Lu, M.; Sleeper, L. A. et al. (2018): Valve-sparing repair with intraoperative balloon dilation in tetralogy of Fallot: midterm results and therapeutic implications. *Journal of thoracic and cardiovascular surgery*, vol. 155, no. 3, pp. 1163-1173.

Jermihov, P. N.; Jia, L.; Sacks, M. S.; Gorman, R. C.; Gorman, J. H. et al. (2011): Effect of geometry on the leaflet stresses in simulated models of congenital bicuspid aortic valves. *Cardiovascular Engineering and Technology*, vol. 2, no. 1, pp. 48-56.

Jonas, S. N.; Kligerman, S. J.; Burke, A. P.; Frazier, A. A.; White, C. S. (2016): Pulmonary valve anatomy and abnormalities: a pictorial essay of radiography, computed tomography (CT), and magnetic resonance imaging (MRI). *Journal of Thoracic Imaging*, vol. 31, no. 1, pp. 4-12.

Kunzelman, K. S.; Einstein, D. R.; Cochran, R. P. (2007): Fluid-structure interaction models of the mitral valve: function in normal and pathological states. *Philosophical Transactions of the Royal Society of London*, vol. 362, no. 1484, pp. 1393-1406.

Li, K.; Sun, W. (2010): Simulated thin pericardial bioprosthetic valve leaflet deformation under static pressure-only loading conditions: implications for percutaneous valves. *Annals of Biomedical Engineering*, vol. 38, no. 8, pp. 2690-2701.

Luraghi, G.; Migliavacca, F.; Matas, J. F. R. (2018): Study on the accuracy of structural and FSI heart valves simulations. *Cardiovascular Engineering and Technology*, vol. 9, no. 4, pp. 723-738.

McAleer, E.; Kort, S.; Rosenzweig, B. P.; Katz, E. S.; Tunick, P. A. et al. (2001): Unusual echocardiographic views of bicuspid and tricuspid pulmonic valves. *Journal of the American Society of Echocardiography*, vol. 14, no. 10, pp. 1036-1038.

Murdock, K.; Martin, C.; Sun, W. (2018): Characterization of mechanical properties of pericardium tissue using planar biaxial tension and flexural deformation. *Journal of the Mechanical Behavior of Biomedical Materials*, vol. 77, pp. 148-156.

Nair, V.; Thangaroopan, M.; Cunningham, K. S.; Mohammed, S. B.; Siu, S. et al. (2006): A bicuspid pulmonary valve associated with tetralogy of Fallot. *Journal of Cardiac Surgery*, vol. 21, no. 2, pp. 185-187.

Rajiah, P.; Nazarian, J.; Vogelius, E.; Gilkeson, R. C. (2014): CT and MRI of pulmonary valvular abnormalities. *Clinical Radiology*, vol. 69, no. 6, pp. 630-638.

Rao, B. N. S.; Anderson, R. C.; Edwards, J. E. (1971): Anatomic variations in the tetralogy of Fallot. *American Heart Journal*, vol. 81, no. 3, pp. 361-371.

Ruckdeschel, E.; Kim, Y. Y. (2019): Pulmonary valve stenosis in the adult patient: pathophysiology, diagnosis and management. *Heart*, vol. 105, no. 5, pp. 414-422.

Sun, W.; Martin, C.; Pham, T. (2014): Computational modeling of cardiac valve function and intervention. *Annual Review of Biomedical Engineering*, vol. 16, pp. 53-76.

Sun, W.; Sacks, M. S.; Sellaro, T. L.; Slaughter, W. S.; Scott, M. J. (2003): Biaxial mechanical response of bioprosthetic heart valve biomaterials to high in-plane shear. *Journal of Biomechanical Engineering*, vol. 125, no. 3, pp. 372-380.

Tang, D.; del Nido, P. J.; Yang, C.; Zuo, H.; Huang, X. et al. (2016): Patient-specific MRI-based right ventricle models using different zero-load diastole and systole geometries for better cardiac stress and strain calculations and pulmonary valve replacement surgical outcome predictions. *PLoS One*, vol. 11, no. 9, e0162986.

Tang, D.; Yang, C.; Geva, T.; Gaudette, G.; Del Nido, P. J. (2011): Multi-physics MRI-based two-layer fluid-structure interaction anisotropic models of human right and left ventricles with different patch materials: cardiac function assessment and mechanical stress analysis. *Computers & Structures*, vol. 89, no. 11-12, pp. 1059-1068.

Tang, D.; Yang, C.; Geva, T.; Del Nido, P. J. (2008): Patient-specific MRI-based 3D FSI RV/LV/patch models for pulmonary valve replacement surgery and patch optimization. *Journal of Biomechanical Engineering*, vol. 130, no. 4, 041010.

Tang, D.; Yang, C.; Del Nido, P. J.; Zuo, H.; Rathod, R. H. et al. (2016): Mechanical stress is associated with right ventricular response to pulmonary valve replacement in patients with repaired tetralogy of Fallot. *Journal of Thoracic and Cardiovascular Surgery*, vol. 151, no. 3, pp. 687-694.

Whitener, S.; Konoske, R.; Mark, J. B. (2014): Pulmonary artery catheter. *Best Practice & Research Clinical Anaesthesiology*, vol. 28, no. 4, pp. 323-335.

Winn, K. J.; Hutchins, G. M. (1973): The pathogenesis of tetralogy of Fallot. *American Journal of Pathology*, vol. 73, no. 1, pp. 157-172.

Yang, C.; Tang, D.; Haber, I.; Geva, T.; Del Nido, P. J. (2007): *In vivo* MRI-based 3D FSI RV/LV models for human right ventricle and patch design for potential computer-aided surgery optimization. *Computers & Structures*, vol. 85, no. 11-14, pp. 988-997.

Zhou, Z.; Geva, T.; Rathod, R. H.; Tang, A.; Yang, C. et al. (2018): Combining smaller patch, rv remodeling and tissue regeneration in pulmonary valve replacement surgery design may lead to better post-surgery RV cardiac function for patients with tetralogy of Fallot. *Molecular & Cellular Biomechanics*, vol. 15, no. 2, pp. 99-115.